

LIDAR STUDIES OF CLOUD FIELDS AND UNDERLYING SURFACE FROM SPACE

V.E. Zuev, Yu.S. Balin, G.G. Matvienko, A.A. Tikhomirov, and V.S. Shamanaev

*Institute of Atmospheric Optics,
Siberian Branch of the Russian Academy of Sciences, Tomsk
Received January 20, 1997*

The first results on laser sensing of cloud fields and of the underlying surface, obtained with the use of the Russian orbital rangefinders and the Balkan lidar placed on board the Spectr module of the Mir space station, are analyzed. It is demonstrated that the multiple scattering contribution should be considered in the interpretation of signals reflected from clouds. The contribution from scattering of different order to signals of the Balkan lidar is estimated by the Monte-Carlo method. It is shown that the single-scattering approximation of the lidar equation is valid only for optical thicknesses no more than 0.5. The field experiments have supported the high accuracy (0.7 m) of measuring distances to clouds and underlying surface as well as the feasibility of determining the optical cloud characteristics at the cloud top and the characteristics of the underlying surface.

Wide potentialities for the study of the atmosphere and the underlying surface, connected with the use of lidars placed on board space vehicles, have motivated the intensive development of spaceborne lidar projects^{1–5} and their practical implementation in the last few years.^{6,8} Thus, the LITE orbital lidar experiment^{1,6} was conducted by NASA from Shuttle on September 10–19, 1994. The Russian lidar Balkan–1 has been operating as part of the Spectr scientific module of the Mir space station since May 20, 1995. The Russian-French lidar ALISSA was launched into orbit as part of the Priroda module of the same space station in May 1996. The first spaceborne lidar measurements, in spite of the large number of model estimates were to a greater extent technological (pilot) than observational in character. Speaking about the Russian spaceborne lidar experience, we note that the history of the lidar study of the Earth from space goes back to 1982, when the laser rangefinders were first launched into orbit.⁷ It turned out that the rangefinders were capable of studying not only the surface, but also the cloudiness, thereby providing the possibility to check lidar algorithms for processing signals from 3-D objects (clouds).

This paper is devoted to an analysis of the results of laser sensing of cloudiness and of the underlying surface obtained with the use of the Russian orbital rangefinders and the Balkan–1 lidar.

LASER SENSING OF THE EARTH USING THE ORBITAL RANGEFINDERS

The orbital rangefinder is intended to measure the exact (with an error of several fractions of a meter) distance between a geodetic satellite and a

sounded surface. Its operation is based on emission of short light pulses, detection of reflected pulses, and determination of the interval between transmission and reception of reflected pulses. However, in an attempt to extend the potentialities of the rangefinders and to increase the reliability of their recording systems, the multithreshold concept of measuring intervals was used instead of a single threshold principle. This has allowed us to reconstruct the reflected signal waveform, which is of special interest for sensing of 3-D media – the atmosphere and the ocean.^{7,9,10} In case of laser sensing of the underlying surface, multithreshold recording systems yield information about the surface tilt from broadening of a reflected pulse.¹¹

The Lora series Russian orbital laser rangefinders⁷ have been operating in space since 1982. Their transeiving systems have the following parameters:

Radiation wavelength, nm	532
Pulse energy, J	0.20
Pulse duration, ns	10
Diameter of the receiving telescope, m	0.27
Angular beam divergence, sec of arc	30
Field-of-view-angle, sec of arc	60
Pulse repetition frequency, Hz	0.18

A recording system of the rangefinder was based on the threshold principle. Four systems that measured pulse duration at four threshold power levels P_1, \dots, P_4 were used. The selected threshold levels are illustrated by Fig. 1, which shows the estimated profiles of the lidar return signal power, in W (the lower horizontal axis) and photons per microsecond (the upper horizontal axis). As seen from the figure, the threshold levels of the rangefinder were chosen so that all types of

underlying surfaces provided signals at all four threshold levels whereas the background signals were less than the lower threshold level. The figure also shows that clouds of intermediate density (whose scattering coefficient is about 10 km^{-1}) and especially the aerosol atmosphere produce signals that are below the least threshold of detection of the lidar return signal duration. Therefore, the orbital rangefinder can detect only signals reflected from dense clouds in addition to signals reflected from the Earth's surface.

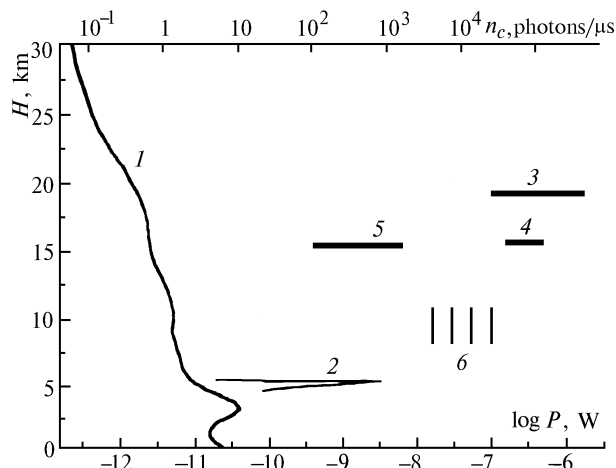


FIG. 1. Model estimates of the power recorded with the laser rangefinder (the orbit altitude was 300 km): 1) cloudless atmosphere, model from Ref. 12; 2) homogeneous cloud at an altitude of 5 km with a scattering coefficient of 10 km^{-1} ; 3) range of variation of signals reflected from the underlying surface; 4) range of variation of signals reflected from the rough sea surface; 5) range of variation of background illumination recorded in the filter bandwidth at a solar zenith angle of 60° (maximum level); 6) threshold levels of the system for measuring threshold pulse duration.

The time in the recording system was counted off from the instant of pulse transmission. The first system for measuring threshold duration was switched on the instant t_1 , when a lidar return signal power $P(t)$ increased to P_1 and switched off at the instant t_2 , thereby determining the threshold pulse duration $\tau_1 = t_2 - t_1$. Other threshold pulse durations $\tau_2 \dots \tau_4$ were measured in the same way. All four threshold duration values $\tau_1 \dots \tau_4$ were recorded when the maximum signal power P_{\max} exceeded P_4 . Only one threshold duration τ_1 was recorded when $P_1 < P_{\max} < P_2$. The distance to a reflecting object was determined from the time T_0 between the instant of sounding pulse transmission and the instant of recording of the center of the highest-threshold duration.

Numerous experiments on laser ranging of the Earth's surface have demonstrated high efficiency of the orbital rangefinders in the cloudless atmosphere. The error in measuring the distance was 0.7 m. In the cloudy atmosphere, the signal reflected from the upper boundary of dense clouds was recorded. In

case of less dense cloudiness we did not observe the signal reflected from the Earth's surface vanished due to its attenuation within the cloudiness.

1-D signals reflected from the Earth's surface were repeatedly analyzed (see, for example, Ref. 11). Therefore, it seems more interesting to us to consider the signals reflected from cloudiness. Below we consider the measurement runs (several successive sensing events with a pulse repetition period of 5.5 s) in which a transition was observed either from sensing of the underlying surface (land or sea) to sensing of the cloudiness or *vice versa*. In these cases, reliable identification of cloudiness is possible and determination of the upper cloud boundary altitude (UCBA) from the change of the time of arrival of the next reflected pulse. A total of 56 sensing events with the UCBA varying from 0.6 to 5 km was analyzed. In 28 events, the signal was recorded only at the first threshold level and only in 5 events the signal was recorded at all four thresholds. The pulse duration at the first threshold level τ_1 was changed from 22 to 200 ns, which corresponded to the cloud sensing depth $r_1 \approx c \tau_1 / 2$ varying in the range from 3 to 30 m.

The difference between the threshold principle of signal recording used in range finding from the amplitude-temporal principle typical of lidars called for the development of special procedure for signal conversion.

The method of lidar signal modeling from a set of discrete threshold duration counts was used. A signal calculated in the single scattering approximation for a horizontally homogeneous cloud provided a basis for the model. The simplest models were used for the cloudiness among them the model of a cloud homogeneous along a sensing path with a preset or unknown lidar ratio and the power-law distribution of the extinction coefficient σ . The values of the parameters were adjusted minimization of the mean square discrepancy of adjustable and actual pulse duration values.

Our estimates have shown that the reconstructed values of σ are within $14\text{--}500 \text{ km}^{-1}$.

This is a very wide range. Figure 2 shows the total probability $f(\sigma)$ of occurrence the extinction coefficient σ reconstructed from our data compared with the data presented in Ref. 13 for clouds of different types. The satisfactory agreement between our data and results of independent measurements for dense Cu clouds confirms the validity of our estimates of σ .

The estimated values of the lidar ratio b deviated from their model estimates larger than σ . Thus, the average value of b was 0.7, and in 25% of all cases $b > 0.1$, that is, much greater than the physically justified values of b for water-droplet clouds.¹⁴ As a rule, this is typical of the lidar pulses having long duration at the lower thresholds (100 ns and longer). These very signals had the poor quality of minimization of their discrepancy when the model parameters were adjusted for the preset values of b .

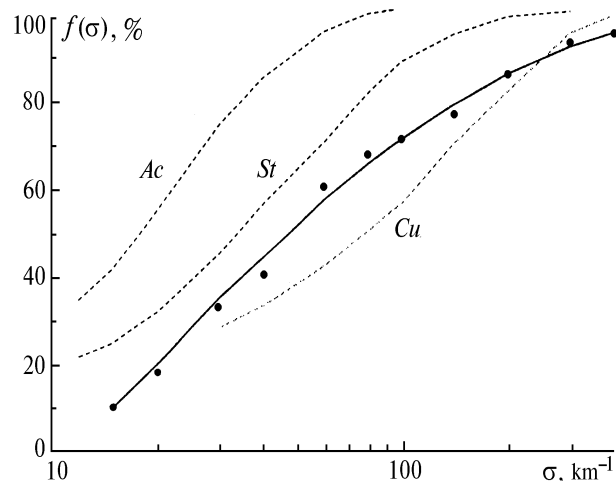


FIG. 2. Total probability $f(\sigma)$ of occurrence of the extinction coefficient σ from the data of all sensing events (solid curve). Dashed curves are plotted from the experimental data of Ref. 13 for clouds of indicated types.

We believe that such overestimated values of b can be explained by a discrepancy between the parameters of actual clouds and of the proposed models. The following hypotheses are most probable: First, the contribution of glint reflections from oriented ice plates concentrated at the cloud top, to lidar return signals. Second, stepwise variation of the UCBA within the laser spot 50 m in diameter, with the step size comparable with the spot diameter. Third, essential contribution from multiple scattering to a lidar return signal. The last is most important. The optical radius of the laser spot at the cloud top R_{opt} , which primarily determines the level of multiple scattering in lidar return signals, reached $R_{\text{opt}} = 1$ for $\sigma = 30 \text{ km}^{-1}$. According to studies performed in Ref. 15, the signal decrement decreased by a factor of 2.6 even at $R_{\text{opt}} = 1.5$ due to the contribution of multiple scattering increasing with time. For our data processing algorithm, we obtain underestimated values of σ and overestimated values of b .

Our results do not contradict cloud physics and can be considered as the first experience in laser sensing of the atmosphere from space. In addition, our estimates confirm that spaceborne lidars can yield physically reliable information about cloud layers. They also provide a basis for guiding the development of special-purpose lidar systems and indicate the necessity of the further improvement of the lidar software considering the actual parameters of broken cumulus clouds and the multiple scattering contribution. Taking into account the importance of estimating the multiple scattering contribution to spaceborne lidar signals, below we analyze numerically the effect of this factor.

ESTIMATE OF THE MULTIPLE SCATTERING CONTRIBUTION TO ORBITAL LIDAR RETURN SIGNALS

Here, the multiple scattering contribution is estimated by the Monte Carlo method, which also provides a possibility of varying the input parameters over wide limits, impossible in field experiments.

The signal power of laser radar, $P(h)$, reflected by a scattering media, depends on the time or the distance to an investigated object.

As a rule, a valid information-bearing signal is considered to be a signal $P_0(h)$ singly scattered in the direction toward an optical detector. In this case, the recorded signal is given by the well-known lidar equation

$$P(h) = W_0 A b \sigma(h) h^{-2} \exp \left\{ -2 \int_0^h \sigma(h') dh' \right\}, \quad (1)$$

where W_0 is the transmitted pulse energy, A is the instrumental function, and $\sigma(h)$ is the volume extinction coefficient depending on the altitude h . By measuring $P(h)$ and using Eq. (1), we can, in principle, derive the information on the optical parameters of investigated medium. The problem is complicated by the background noise accompanying the operation of any transceiving system. The sources of noise have various origin. In our case, we are interested in the active noise produced by the signal itself or caused by multiple scattering within the angular aperture of the receiver. In general, the backscatter signal power is a sum of two additive components

$$P(h) = P_0(h) + P_{\text{bg}}(h),$$

where $P_0(h)$ is the singly scattered signal and $P_{\text{bg}}(h)$ is the multiple scattering contribution.

The component $P_0(h)$ can be found from Eq. (1) and $P_{\text{bg}}(h)$ can be found by solving the nonstationary radiative transfer equation. The Monte Carlo method^{16,17} is most suitable for solving this radiative transfer equation with initial and boundary conditions and for estimating separately the contributions from scattering of different orders. The problem was formulated as follows. A monostatic laser radar was at the altitude $H = 400 \text{ m}$ above the Earth's surface (corresponding to the orbit altitude of the Mir space station).

A source radiated isotropically within the given cone of directions $2\pi(1 - \cos\varphi_s)$, where $\varphi_s = 0.2 \text{ mrad}$. A return signal was recorded by a detector within the cone $2\pi(1 - \cos\varphi_d)$, where $\varphi_d = 0.44 \text{ mrad}$. The calculations were done for a rectangular pulse with a duration of 10 ns and energy $W_0 = 1 \text{ J}$. The total efficiency of the entire transceiving system was $k_{\text{eff}} = 1$. A cloud layer was Deirmendjian's C1 or C2 cloud¹⁴ within the 1.5–2-km altitude range. We considered continuous stratified clouds. The aerosol radiation

extinction was considered in the 30-km layer of the atmosphere just above the cloudiness. The altitude profiles of the optical parameters in this layer were taken for the background aerosol model suggested in Ref. 18. The scattering properties were described by Deirmenjian's H haze model.¹⁴

The cloud layer was divided into n sublayers of thicknesses Δh . Their extinction coefficients $\sigma(h_i)$ changed from sublayer to sublayer, remaining constant within the sublayer Δh_i .

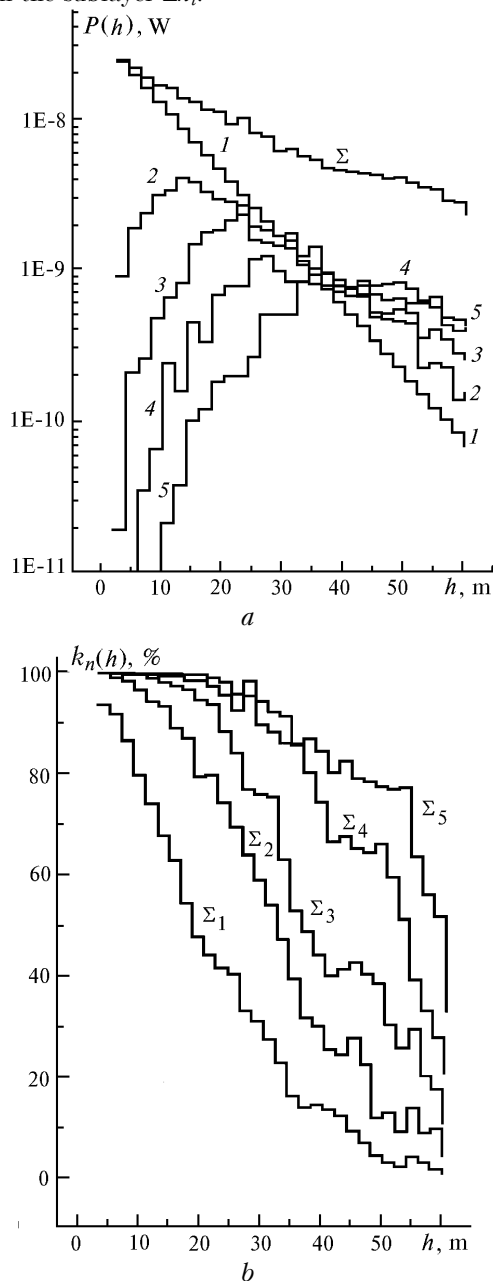


FIG. 3. Estimated contributions from multiple scattering in case of sensing of the homogeneous C1 cloud: a) total signal power Σ and powers of signals of different scattering multiplicity (indicated by the numbers adjacent to the curves); b) ratios of powers of signals of different scattering multiplicity to the total signal power, in percent.

Below we discuss the lidar return signal power $P(h)$ calculated for clouds with different profiles of $\sigma(h)$ within the cloud. Calculations were done by M.M. Krekova considering the actual parameters of the Balkan-1 lidar. They essentially complement and refine the estimates reported in Ref. 15. The parameter $h = ct_i/2$ is plotted in Figs. 3 and 4 as the abscissa. It specifies the accumulated photon paths, where t_i are the photon transit times within the cloud. The results are presented for one field-of-view angle, because its variations affect only slightly the behavior and the level of the lidar return signal $P(h)$ in case of spaceborne lidar sensing, as demonstrated previously in Ref. 15. The calculated results are given for the cloud top and optical depths $\tau \sim 2-3$.

Figure 3 illustrates the results calculated for the homogeneous optically dense cloud with $\sigma(h) = \text{const} = 50 \text{ km}^{-1}$. Despite the high optical density of the cloud, the lidar return signal decreases monotonically by an order of magnitude. The reason for the slow signal decay is the high level of multiple scattering background caused by larger scattering volume enclosed within the viewing cone. The contribution from the singly scattered signal predominates at $\tau \leq 0.8$. Then the contribution from the higher-order scattering increases, and becomes comparable with the contribution of single scattering, at $\tau \sim 1.2-1.6$. At $\tau \sim 2.5-3$, the contribution from signals whose scattering order $n > 4$ starts to increase. Figure 3b shows the ratio of the singly scattered signal power to the total signal power, in percent (curve Σ_1), the ratio of a sum of singly and doubly scattered signal powers to the total signal power (curve Σ_2), in percent, and so on. It can be seen that more than 60% of the total power comes from the single and double scattering up to $\tau \sim 1.5$ and only a sum of five scattering orders allows us to consider most of the power coming to the detector from depths $\tau \sim 2.5-3$.

Our calculations for C2 cloud model, having much less asymmetry of the scattering phase function, demonstrate analogous signal patterns. Only some differences in the absolute values of the scattered power of multiplicity $n > 3$ have been found. This is primarily due to the fact that the laser beam radii at the cloud top ($R_b \sim 100 \text{ m}$) are comparable with the cloud layer thickness. As a consequence, the radiation scattered in the side directions remains practically within the viewing cone and contributes to the diffusely reflected radiation flux.

Figure 4 shows the results of calculations for the inhomogeneous cloud. The calculations were done for the profile of the extinction coefficient $\sigma(h)$ being typical of stratified clouds, namely, the parabolic profile that increases fast starting from the cloud top and then decreases slowly toward the cloud base.¹⁹ To observe the fine structure of the extinction coefficient profile, the signal should be integrated over short intervals. Most of the calculations were done with $\Delta h = c \Delta t/2 = 2-3 \text{ m}$.

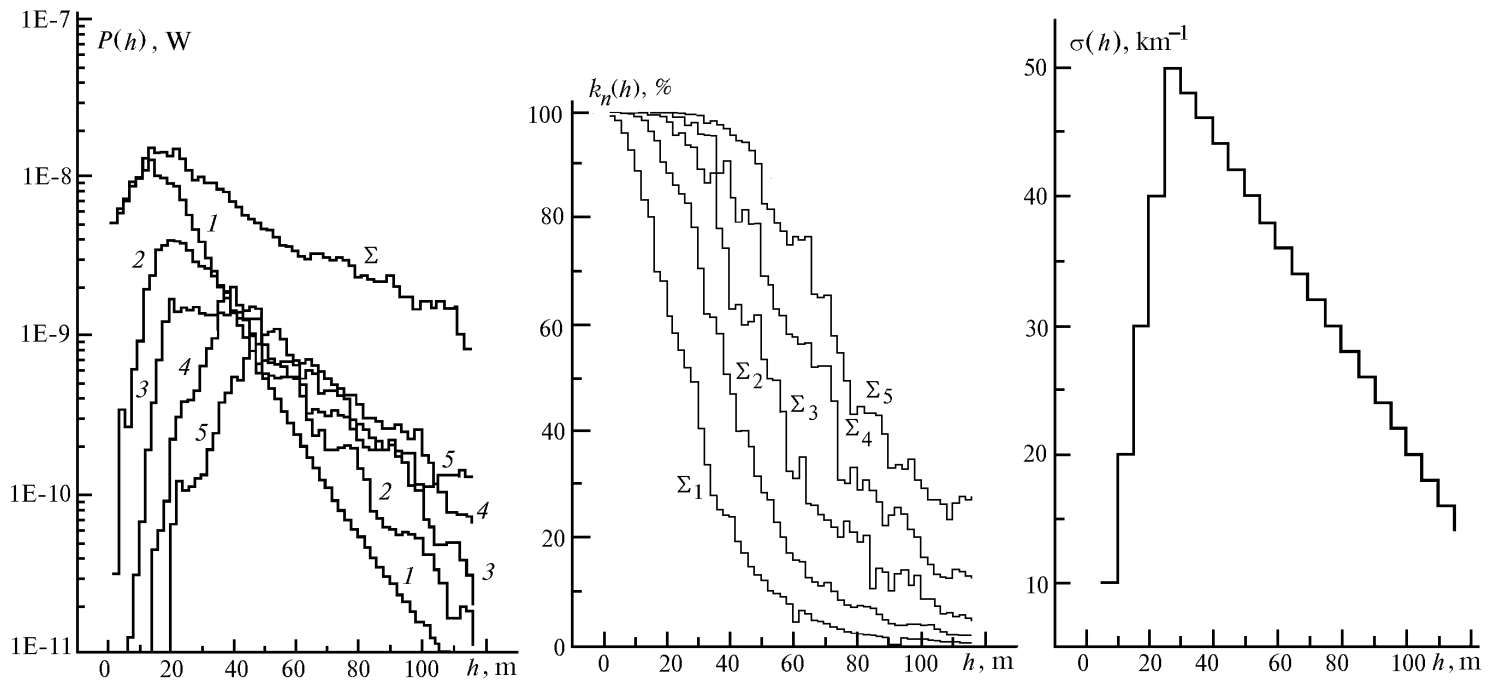


FIG. 4. Same as in Fig. 3 but for inhomogeneous cloud with the profile of the scattering coefficient $\sigma(h)$ illustrated by figure c.

As is seen from Fig. 4, the maximum of the signal $P(h)$ is shifted toward smaller depths and practically coincides with the maximum of the singly scattered signal. As in the case of the homogeneous cloud the contribution from scattering of higher orders to the total signal becomes significant starting from $\tau \sim 1.5$. An analysis of the calculated results has demonstrated that the leading edge of the pulse up to $\tau \sim 0.8 - 1$ is formed by low-order scattering, regardless of the profiles of the cloud extinction coefficient.

The higher is the scattering multiplicity the smaller is its contribution to the absolute signal level. At $\tau \sim 0.8 - 1.5$, the contribution of higher-order scattering increases and roles of scattering of different orders change. The contributions from the first five orders of scattering to the signal $P(h)$ become comparable in their absolute values at $\tau \sim 1.5 - 1.8$. The trailing edge of the pulse (at $\tau > 2$) is formed primarily due to scattering of higher orders. Calculations for the C2 cloud model with the profile of $\sigma(h)$ shown in Fig. 4 have shown that the signals $P(h)$ practically coincide for two cloud types that differ in their particle size distribution functions. This is also due to the fact that the scattering phase functions of these cloud types are practically the same for the scattering angles close to 180° .

On the basis of these estimates we can state the following. In the interpretation of lidar return signals, it should be taken into account that the single-scattering contribution predominates up to $\tau \sim 0.4 - 0.5$ (corresponding to the geometric cloud thickness up to several tens of meters); therefore, lidar equation (1) is valid within these limits. Consideration of the double-scattering contribution extends these limits of applicability of the lidar equation up to $\tau \sim 0.8 - 1$. Polarization sensing with subsequent filtration of the background signal component also extends the above-indicated limits of applicability of Eq. (1). Filtration makes sense only up to $\tau \sim 2$, when the singly scattered signal level is still high.

SPACEBORNE EXPERIMENTS ON SENSING OF CLOUD FIELDS AND UNDERLYING SURFACE USING THE BALKAN LIDAR

The Balkan spaceborne lidar is intended for sensing of the underlying surface and the upper cloud boundary.⁸ To develop this lidar, we used the accumulated experience in the development of ground-based, airborne, and spaceborne lidars. This lidar comprises the systems and units that have been approved for the orbital rangefinders. The lidar transceiver has the same parameters as the rangefinder transceiver. A digital system for signal recording was developed on the basis of a 6-bit analog-to-digital converter with a sampling frequency of 50 MHz (a spatial discretization step of 3 m). The lidar preserved the range-finding channel. The data of sensing were telemetered to ground-based stations where they were completely processed. The energy consumption of the

lidar is low (200 W), so it can operate simultaneously with other systems and devices of the Mir space station.

The power of signals detected by the range-finding channel is shown in Fig. 1. The lidar channel had a minimum threshold signal power of about $4 \cdot 10^{-9}$ W, that is, the digital lidar channel had higher sensitivity. However, the contribution from the background illumination also increased.

By now we have performed two spaceborne experiments in August–September 1995 and February–April 1996. At that time, the orbital parameters were as follows: 393 km at apogee, 413 km at perigee, the average period of revolution around the Earth was 92.41 min, the orbit was at an angle of 51.74° to the equator, and the mean rotational velocity of the space station was 7.7 km/s. The laser spot diameters on the Earth's surface were no greater than 100 m for this orbit, and their centers were spaced at 42.58 km. Most of the experimental data were obtained over the North Atlantic, the Pacific Ocean, the Indian Ocean, and Australia.

The data processing algorithm for the range-finding channel includes a comparison between the measured distance D_{meas} and the calculated distances $D_{\text{calc}}(t)$ for corresponding times to eliminate erroneous signals produced by the background illumination. Erroneous triggering the threshold system of the range-finding channel may occur when the amplitude of a background noise pulse exceeds the first threshold and the noise pulse itself falls within the strobe pulse of a time-code converter. Erroneous triggering was discriminated by two criteria: either D_{meas} exceeded D_{calc} by the amount greater than the systematic measurement error, or D_{meas} was less than $(D_{\text{calc}} - 12 \text{ km})$, which is the case for signals reflected from the objects located at altitudes $> 12 \text{ km}$ above the Earth's surface.

Our spaceborne experiments demonstrated that the threshold system was triggered erroneously most often above the illuminated side of the Earth (up to 50% in a measurement session). Erroneous triggering was also observed above the dark side of the Earth when the Moon phase exceeded 0.9 (no more than 3%).

The amplitudes of lidar returns from low-dense clouds with small gradient of scattering coefficient usually did not exceed the first threshold level. This case was considered as the lack of signal, and the signal from the Earth's surface was not recorded.

The profiles of the upper cloud boundary altitude and of the underlying surface measured with the range-finding channel of the Balkan lidar when the space station orbited above the dark side of the Earth are shown in Fig. 5. The lidar axis was oriented in the nadir (so-called orbital coordinate system (OCS) regime of orientation of the space station in flight). The difference between the calculated (from the ballistic data of the Flight

Control Center) and measured distances is plotted on the ordinate and the serial number of the measurement run in the sensing session is plotted on the abscissa. The geographic coordinates of the

first and last points of the sensing path are also indicated on the abscissa. The total length of the examined path was more than 2500 km.

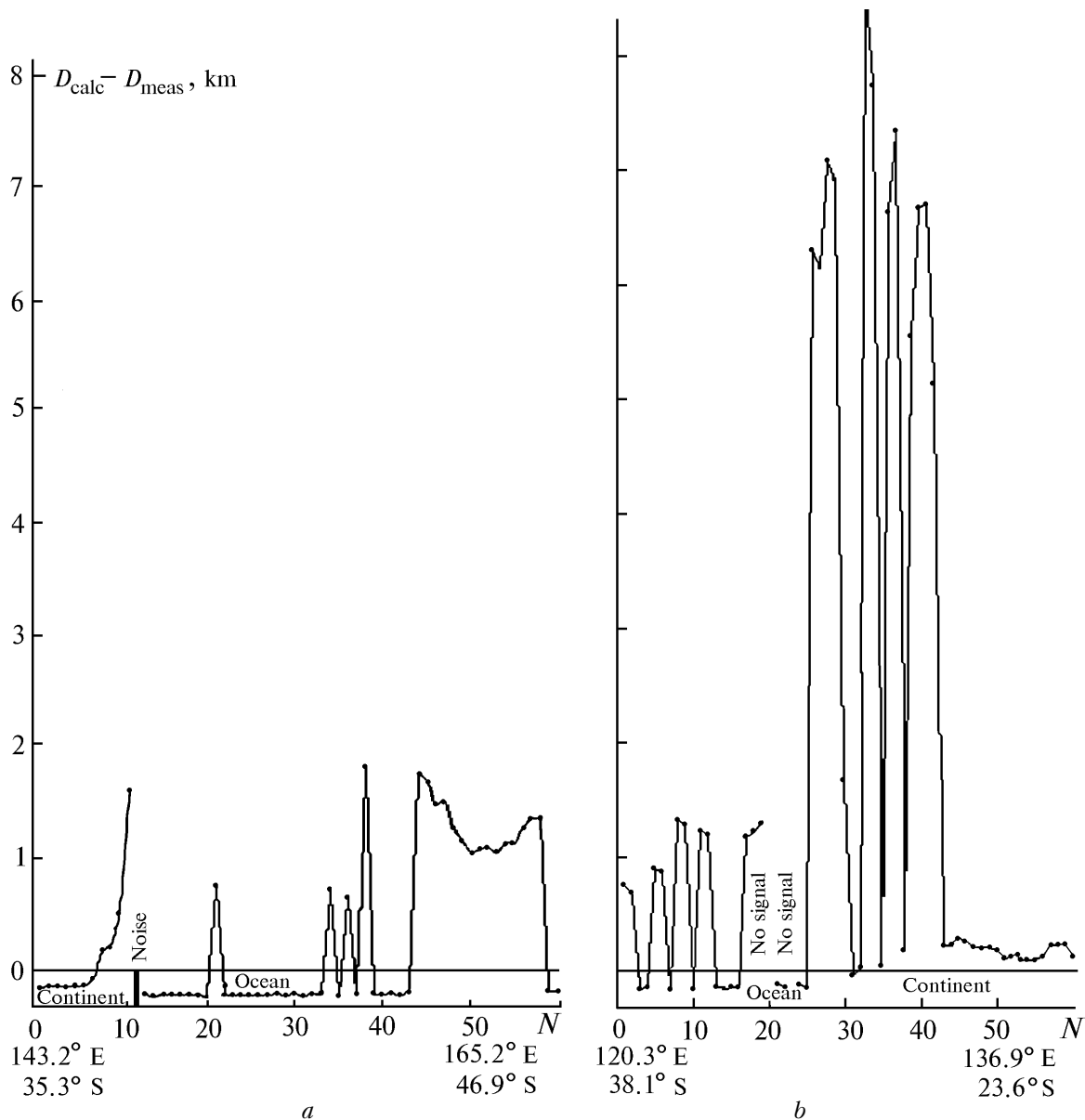


FIG. 5. Profiles of the upper cloud boundary altitude and of the underlying surface measured with the lidar on 5 March (a) and 31 March (b) 1996. The lidar axis was oriented in the nadir.

In the sensing session on 5 March 1996 from 15:42:02 to 15:47:28, Moscow summer time (MST), the first 12 sensing runs were performed over Australia (Fig. 5a). The profile of the Great Dividing Range (with mountains as high as 2000 m) located near the coast of the continent, was recorded. Sensing was performed in full Moon. During the session, the Moon elevation angle changed from 43.1° to 40.3° .

As pointed out in Ref. 23, when sensing sessions were carried out for Moon phases > 0.9 , the background noise signal was recorded above the coastal marine zone (in this case, the amplitude of the

background noise signal exceeded the first threshold of the lidar range-finding channel and when it was within the strobe of the time-code converter, it was recorded as a valid signal). The criterion for the elimination of these cases was the value of the recorded distance D_{meas} , which deviated strongly from the general behavior of measurable series of the parameter D_{meas} (see Ref. 21). Then when the space station flew above the Tasman Sea, sparse clouds were recorded followed by the continuous cloudiness with the UCBA varying from 1.1 to 1.8 km. The cloud field terminated above the south end of New Zealand.

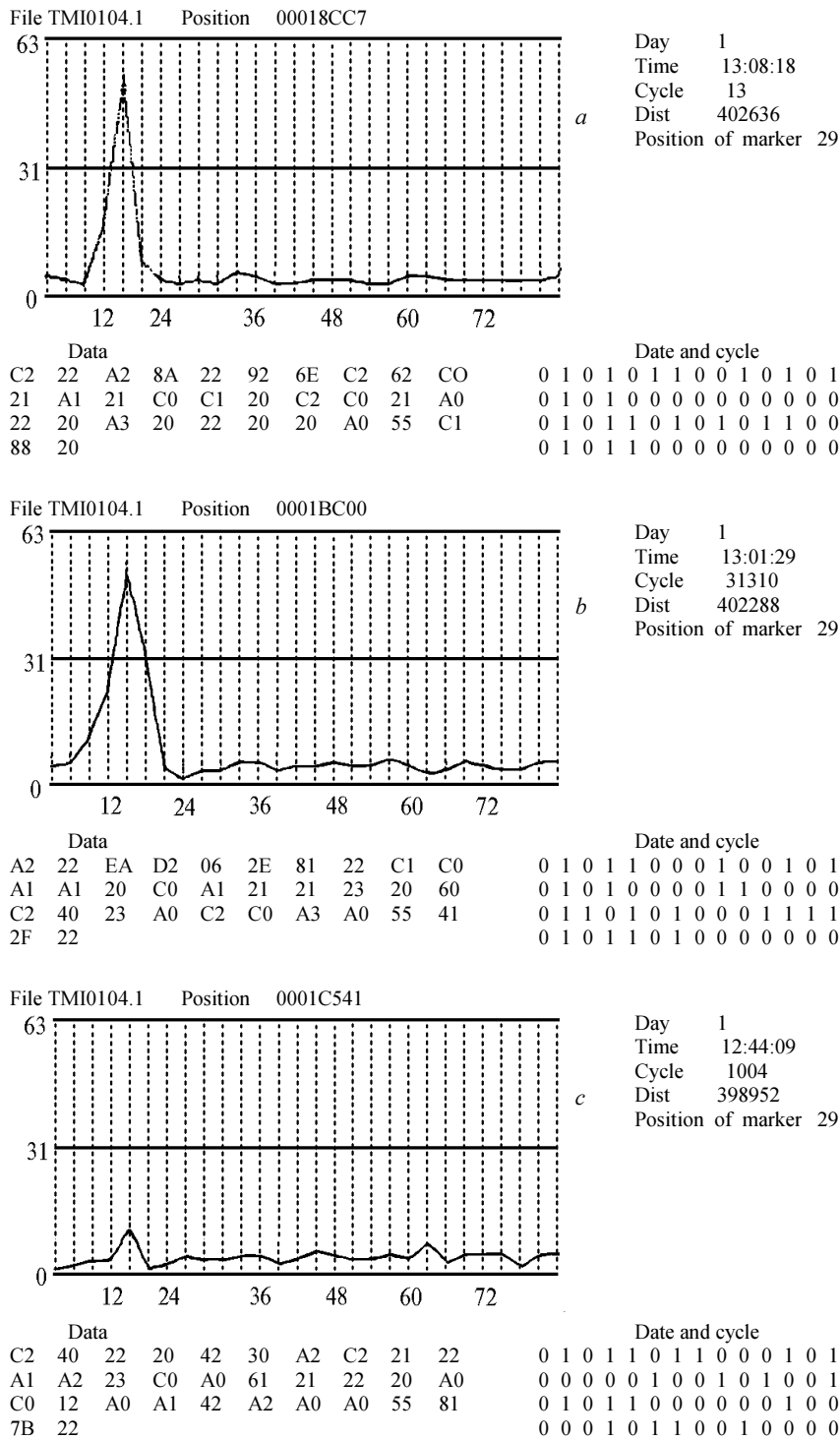


FIG. 6. Lidar signals recorded during the sensing session on 1 April 1996 from the underlying surface (a and b) and cloud (c).

Sensing on 31 March 1996 from 14:03:56 to 14:09:02, MST (see Fig. 5b) was performed when the space station flew above the dark side of the Earth from southwest to northeast (from the eastern part of the Indian Ocean to the central part of the Australian continent). The Moon phase was 0.87 and its elevation angle changed from 33.7° to 54.4°. In this case, the

range-finding lidar channel recorded sparse low cloud fields above the Indian Ocean and high cloud fields above the continent. When the lidar return signal amplitude was less than the first threshold, the lack of the signal was registered. It should be noted that analogous cloud fields were also recorded above the Australian continent in other sensing sessions.

A procedure for signal processing included the following stages: 1) filtration (selection of a valid signal), 2) classification (identification of a sounded object type), and 3) estimation of the object parameters.

The significant independent parameters of a lidar return signal, which describe reliably the sounded objects, where chosen as discriminating parameters for object classification: the duration of the leading pulse edge, the distance to the object, and the integral S -function of the lidar return signal ($S = P \cdot h^2$). These parameters carry information about the physical state of the sounded object because their values are of interest for meteorology, climatology, and refinement of the procedure for calculating the orbital parameters. The upper cloud boundary altitude, the distance to the Earth's surface, and the optical parameters of the underlying surface and cloudiness also can be considered as discriminating parameters. For example, the integral S -function is directly related to the reflecting properties of clouds and the underlying surface.

Under assumption of a linear increase in the scattering coefficient $\sigma(h)$, we obtain

$$\frac{d\sigma}{dh} = \frac{1}{2(h_m - h_0)^2} = \ln \left(\frac{h_2 - h_0}{h_1 - h_0} \right) [(h_2 - h_0)^2 - (h_1 - h_0)^2]^{-1},$$

which implies that $S(h)$ is related to the gradient $d\sigma/dh$. The estimate of the gradient can be obtained by the least-squares method, that is,

$$\frac{d\sigma}{dh} = \int_{h_1}^{h_2} \ln \left(\frac{h - h_0}{h_m - h_0} \frac{S(h_m)}{S(h)} \right) [(h - h_0)^2 - (h_m - h_0)^2] dh \times$$

$$\times \left\{ \int_{h_1}^{h_2} [(h - h_0)^2 - (h_m - h_0)^2]^2 \right\}^{-1}.$$

Here h_0 and h_m are distances to the starting point of a sounded path and to the signal maximum, respectively, h_1 and h_2 are the distances of equal signal amplitudes in the leading and trailing edges of a lidar return signal ($h_1 < h_2$).

As our model calculations have shown and our experiments have confirmed, stability of the obtained solution worsens when the trailing edge of the lidar return signal is processed. In addition, considering the fact that the trailing edge of the signal comprises the multiple scattering background, we can recommend only the parameters of the leading pulse edge to estimate the average cloud scattering coefficient.

Typical deciphered lidar returns recorded with the lidar channel in the sensing session on 1 April 1996 are shown in Fig. 6. A special computer code²¹ was used to decipher lidar signals recorded as part of a large digital array of telemetric data. The ADC counts are plotted on the ordinate of the figures showing the signal waveform. The distance, in meters (within the recorded object), is plotted on the abscissa. The distance to the sounded object, in meters, is given to the right of the figures among the deciphered passport parameters of the signal and is indicated as Dist. As seen from the figure, the amplitude of the signal reflected from the underlying surface is several times greater than the cloud signal amplitude. Broadening of the signal shown in Fig. 6b is likely due to reflection from a tilted surface. The cloud signal is rather short and has small amplitude, which makes difficult taking full advantage of possible algorithms of cloud signal processing. For this reason, we hereafter use simple algorithms considering the signal amplitude and signal edges.²

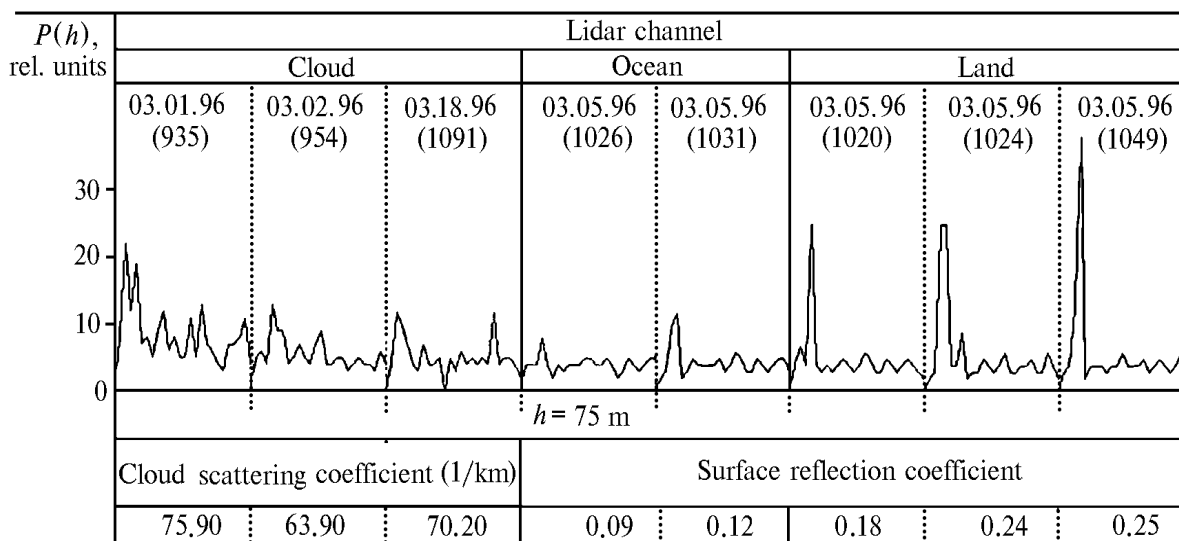


FIG. 7. Examples of lidar return signals from indicated scattering objects and results of reconstruction of their parameters (the figures in parentheses indicate the serial number of the measurement run).

Figure 7 shows the processed lidar signals from reflecting objects of different types (clouds, sea surface, or land). Here, the signal amplitude in units of code of the ADC is plotted on the ordinate and the distance within the sounded object is plotted on the abscissa. As seen from this figure, the signals from clouds and the underlying surface are more intense. Most of the lidar signals were recorded from dense cloud fields, which is vividly illustrated by the magnitudes of the scattering coefficients shown in the figure. The signals from the sea surface and less dense clouds were close to the minimum detectable level and were accompanied with noise. This is indicative of the fact that the potential of the Balkan lidar is still insufficient to investigate the optical cloud parameters and water surface for the given orbit altitude. However, the increase of the spaceborne lidar potential is very expensive because it is connected with the increase of the weight of lidar units and lidar energy supply. Therefore, it is expedient to develop special data processing algorithms for noise suppression.

Our results can be considered as the start of spaceborne lidar sensing of the Earth. They confirm the feasibility of obtaining reliable information about cloud fields and the underlying surface. They also demonstrate the necessity of refinement of mathematical methods for lidar signal processing considering real characteristics of sounded objects and contributions from multiple scattering and noise background. In addition, our accumulated experience in spaceborne lidar sensing is of interest for guiding the development of future lidar systems and their accuracy characteristics as well as for lidar data interpretation.²²

REFERENCES

1. M.P. McCormic, D.M. Winker, E.V. Browell et al., *Bulletin Meteorol. Soc.* **74**, No. 2, 205–214 (1993).
2. *Backscatter Lidar*, Report ESA SP–1121, ISBN 092–9092–056–4, ATLID Consultant Group, 1990, 27 pp.
3. V.M. Sakharov, ed., *Laser Sensing of the Atmosphere from Space* (Gidrometeoizdat, Leningrad, 1988), 215 pp.
4. Yu.S. Balin, V.V. Burkov, I.V. Znamenskii, et al., in: *Abstracts of Reports at the 15th Intern. Laser Radar Conf.*, Tomsk (1990), Vol. 1, pp. 12–14.
5. *International Special-Purpose Space Project Priroda. Scientific Program of Experiments* (IRE RAS, Moscow, 1991), 136 pp.
6. D.M. Winker, R.M. Couch, and M.P. McCormic, *Proc. IEEE* **84**, 1–17 (1996).
7. G.P. Kokhanenko, G.G. Matvienko, V.S. Shamanaev, et al., *Atmos. Oceanic Opt.* **7**, No. 7, 517–521 (1994).
8. Yu.S. Balin, V.E. Mel'nikov, A.A. Tikhomirov, et al., *Proc. SPIE Lidar Techniques for Remote Sensing* **2310**, 144–151 (1994).
9. Ch. Werner, G. Kokhanenko, G. Matvienko, et al., *Optical Review* **2**, No. 3, 221–224 (1995).
10. G.G. Matvienko, G.P. Kokhanenko, V.S. Shamanaev, et al., *Proc. SPIE Lidar Technique for Remote Sensing* **2310**, 122–128 (1994).
11. J.L. Bufton, *Proc. IEEE* **77**, No. 3, 463–477 (1989).
12. V.M. Orlov, I.V. Samokhvalov, G.M. Krekov, et al., *Signals and Noise in Laser Detection and Ranging* (Radio i Svyaz', Moscow, 1985), 264 pp.
13. E.M. Feigel'son, ed., *Radiation in the Cloudy Atmosphere* (Gidrometeoizdat, Leningrad, 1981), 280 pp.
14. D. Deirmendjian, *Electromagnetic Scattering on Spherical Polydispersions*, Elsevier, Amsterdam; American Elsevier, New York (1969).
15. G.M. Krekov, M.M. Krekova, and I.V. Samokhvalov, *Izvest. Zemli iz Kosmosa*, No. 2, 44–51 (1988).
16. G.I. Marchuk, ed., *The Monte Carlo Method in Atmospheric Optics*, Springer, Berlin (1980).
17. G.M. Krekov, G.A. Mikhailov, and B.A. Kargin, *Izv. Vyssh. Uchebn. Zaved., Fizika*, No. 5, 54–59 (1968).
18. V.E. Zuev and G.M. Krekov, *Optical Models of the Atmosphere* (Gidrometeoizdat, Leningrad, 1986), 256 pp.
19. L.S. Dubrovina, *Clouds and Precipitation from the Data of Airborne Sensing* (Gidrometeoizdat, Leningrad, 1982), 216 pp.
20. B.V. Kaul' and I.V. Samokhvalov, *Izv. Vyssh. Uchebn. Zaved., Fizika*, No. 8, 95–100 (1975).
21. Yu.S. Balin, A.A. Tikhomirov, and S.V. Samoilova, *Atmos. Oceanic Optics* **10**, No. 3, 209–220 (1997).
22. V.E. Zuev, Yu.S. Balin, V.V. Zuev et al., *Atmos. Oceanic Optics* **8**, No. 12, 949–954 (1995).